In vivo imaging with a flat, lensless microscope: supplemental document

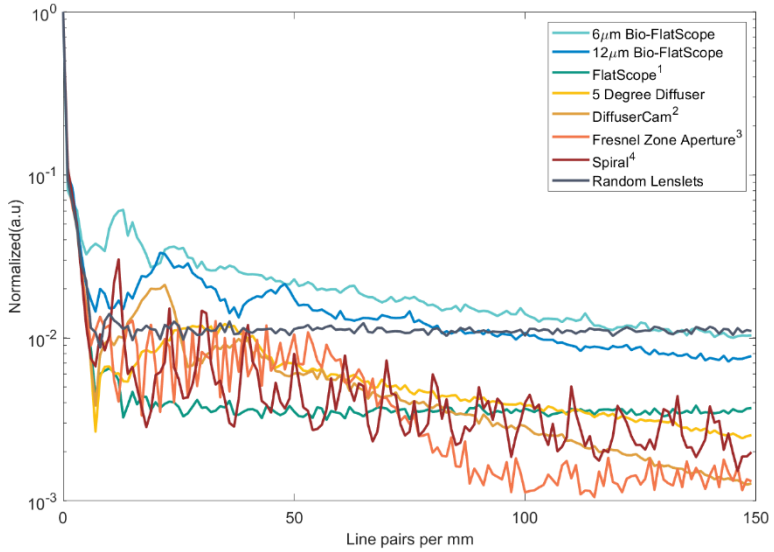

Fig. S1. Modulation transfer function (MTF) comparison among PSF designs used by lensless imaging systems.

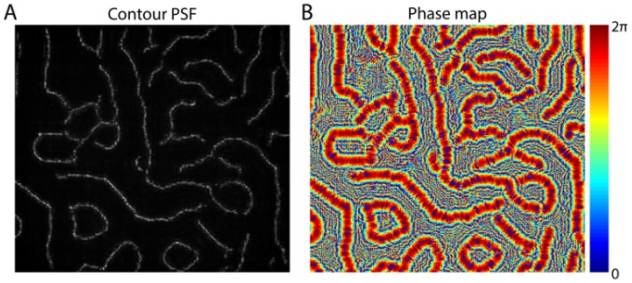

Fig. S2. (A) Contour-based PSF design provides robustness to noise and capturing many directional filters. (B) Phase map for the mask in order to produce the PSF on the image sensor.

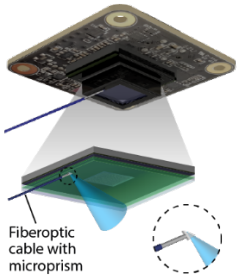

Fig. S3. Bio-FlatScope with near-epi illumination with microprism and fiber-optic cable.

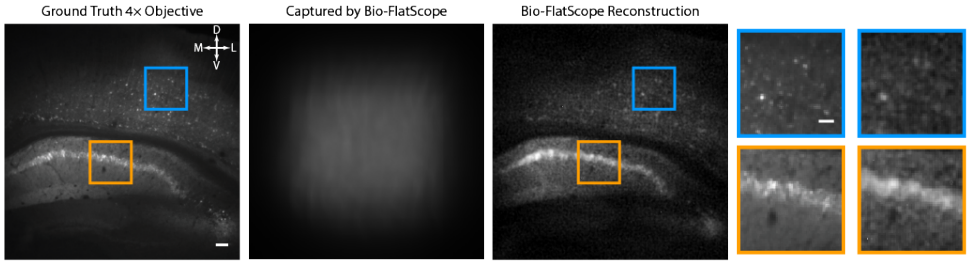

Fig. S4. Mouse brain slice imaging. Ground truth capture, raw capture by Bio-FlatScope, and Bio-FlatScope reconstruction of a mouse brain slice expressing GCaMP6f. The compass shows dorsal-D, ventral-D, medial-M and later-L directions. Scale bar, 100 µm. Far right shows zoom-in comparisons of ground truth and Bio-FlatScope reconstructions, respectively. Scale bar, 50 µm.

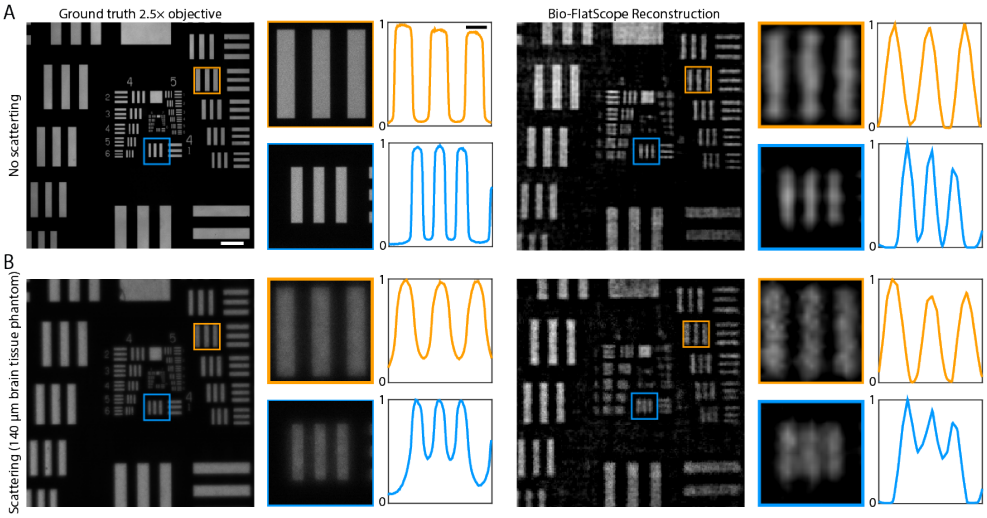

Fig. S5. Imaging through scattering medium. (A) Ground truth (left, captured with a 2.5× objective and Bio-FlatScope reconstruction (right, captured at ~8.5 mm from the device) of USAF 1951 resolution target. Scale bar, 250 µm. Zoom-ins are shown for Group 3 element 3 and group 4 element 1. Scale bar, 50 µm. (B) Ground truth (left, captured with a 2.5× objective) and Bio-FlatScope reconstruction (right, captured at ~8.5 mm from the device) of USAF 1951 resolution target captured through 140 µm of brain tissue phantom. Scale bar, 250 µm. Zoom-ins are shown for Group 3 element 3 and group 4 element 1. Scale bar, 50 µm.

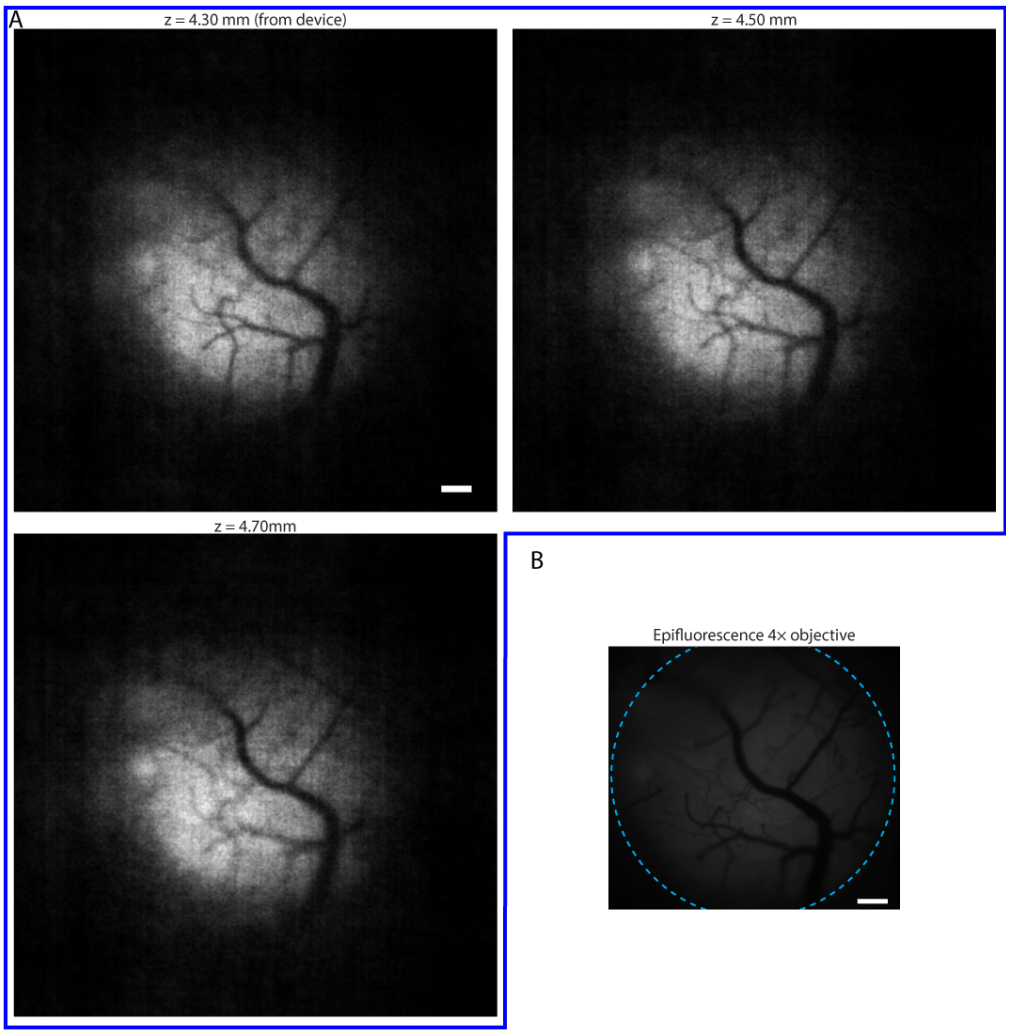

Fig. S6. Full Bio-FlatScope field of view for *in vivo* mouse brain recordings. (A) Full FOV Bio-FlatScope reconstructions of mouse brain *in vivo* at 4.3 mm, 4.5 mm, and 4.7 mm from the device. Dark areas (around edges) are regions located outside of the cranial window. Scale bar, 250 μm (B) Epifluorescence image of same region of the mouse brain captured with a 4× microscope objective. Dashed cyan line indicates the outer edge of the cranial window. Scale bar, 250 μm.

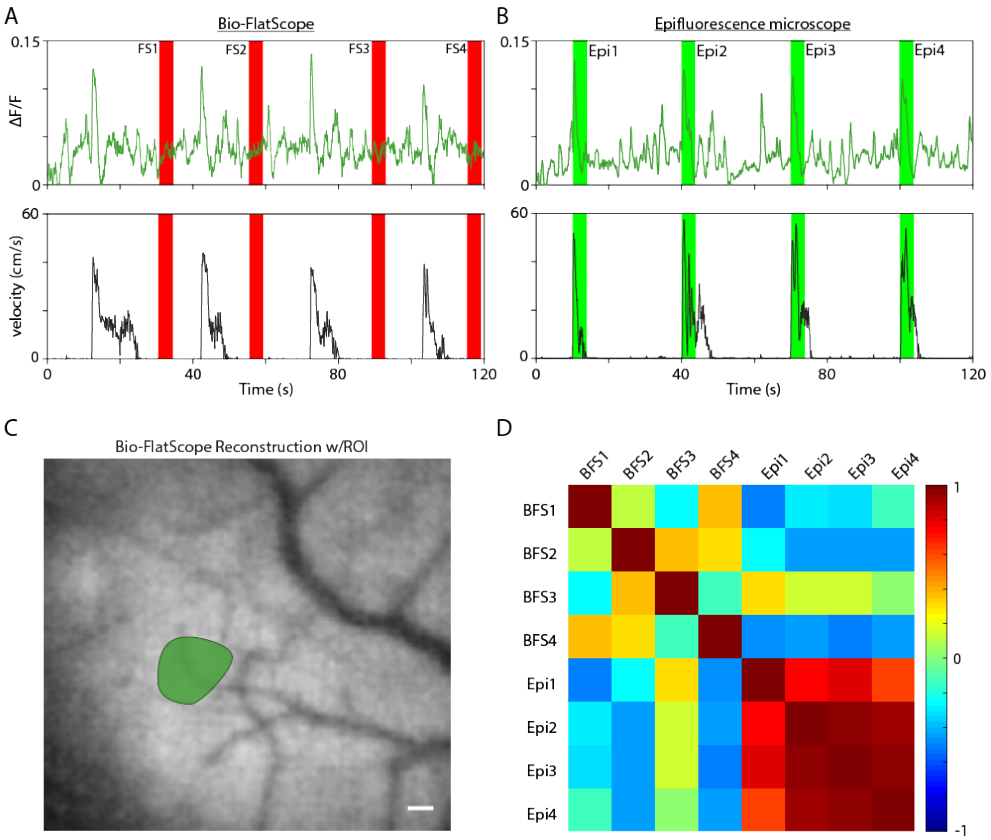

Fig. S7. Comparison of Bio-FlatScope Ca^{2+} responses during stationary periods to stimulus-evoked responses in epifluorescence recordings. (A) ΔF/F trace and treadmill velocity for Bio-FlatScope during recording session. The 4-second windows are selected when the mouse is stationary (having a velocity < 1 cm/s), shown in red. (B) ΔF/F trace and treadmill velocity for epifluorescence during recording session. The rising edge of the 4-second windows in green correspond to the application of tactile stimuli. (C) Bio-FlatScope reconstruction with a single ROI of high-activity marked. Scale bar, 100 μm. (D) Correlation matrix comparing the 4-second windows of little to no movement (red) and stimulus response activity (green). (BFS - Bio-FlatScope, Epi-Epifluorescence microscope).

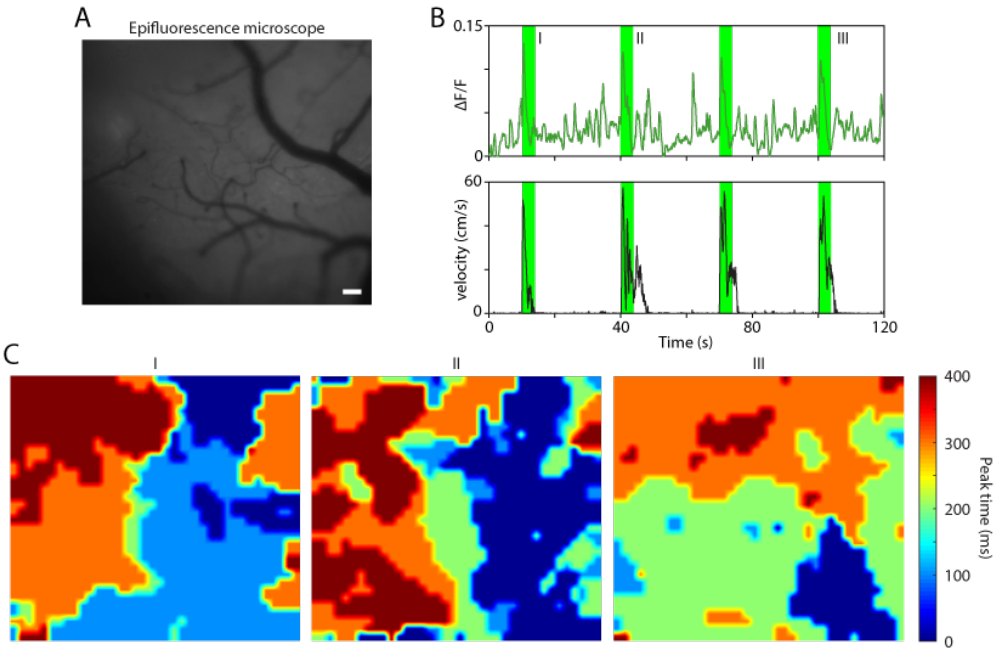

Fig. S8. Spatiotemporal Ca^{2+} dynamics from epifluorescence recording. (A) Single frame from epifluorescence microscope capture of ROI. Scale bar, 100 μm. (B) ΔF/F trace and treadmill velocity for epifluorescence during recording session. The rising edge of the 4-second windows in green correspond to the application of tactile stimuli. (C) Heat maps for epifluorescence captures showing spatiotemporal Ca^{2+} dynamics time-aligned with stimuli (at I, II, and III). Colormap shows the time at which pixels have their peak response for ΔF/F during a 400 ms period.

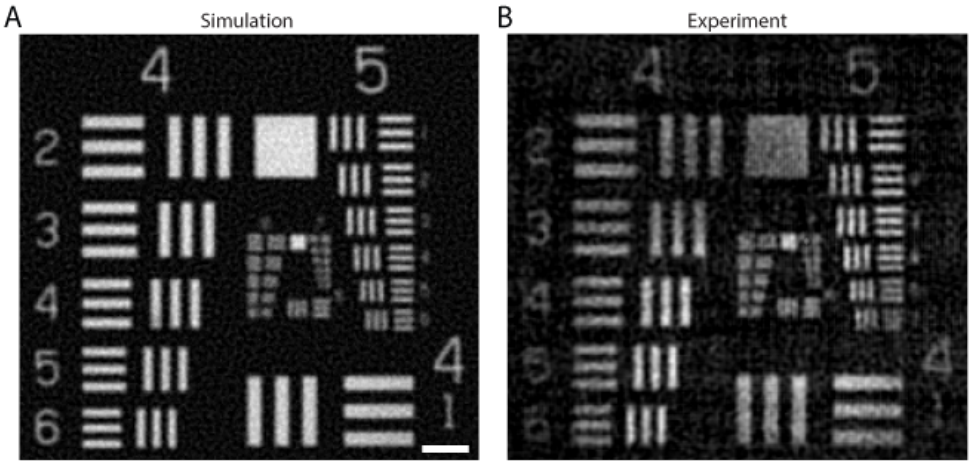

Fig. S9. Simulation vs experimental result of USAF. (A) Simulated Bio-FlatScope reconstruction of USAF target at 4.15 mm from device. Scale bar, 100 μm. (B) Experimental Bio-FlatScope reconstruction of USAF target at the same distance from device. The simulation result shows a very close match to the experimental result with group 5 element 6 being resolved.

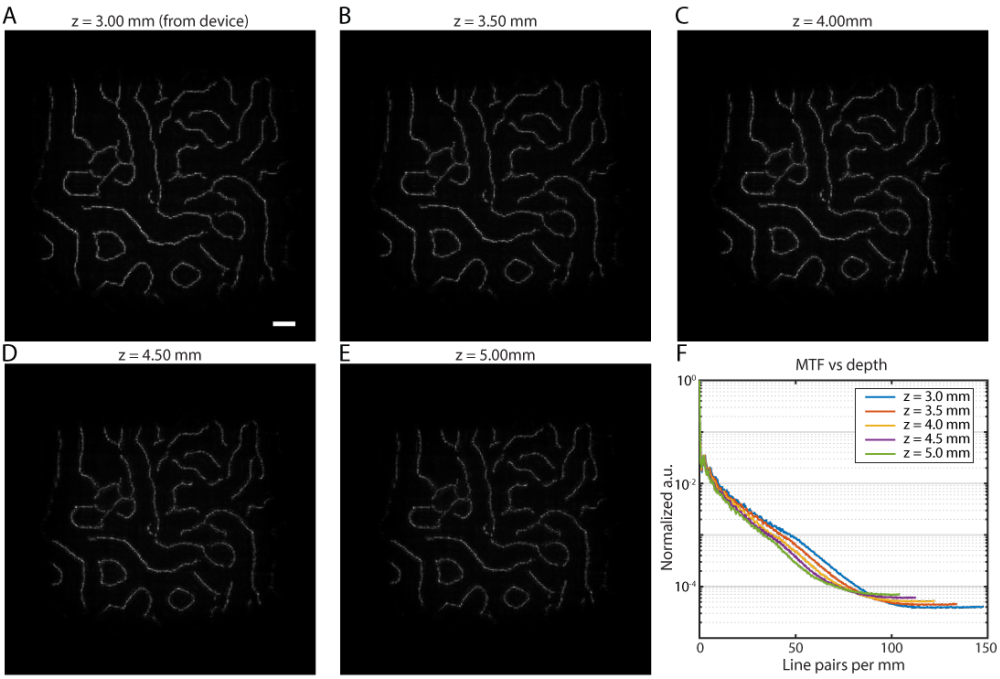

Fig. S10. Captured Bio-FlatScope point spread functions. Bio-FlatScope PSFs captured by imaging a 10 μm fluorescent microsphere (see *Methods*) at different depth planes of (A) 3.00 mm, (B) 3.50 mm, (C) 4.00 mm, (D) 4.50 mm, and (E) 5.00 mm. Scale bar, 100 μm. (F) Computed MTF from PSFs at different depths from Bio-FlatScope. We observe that the resolution decreases with increasing depth, as seen from the shifting of MTF curves to the left.

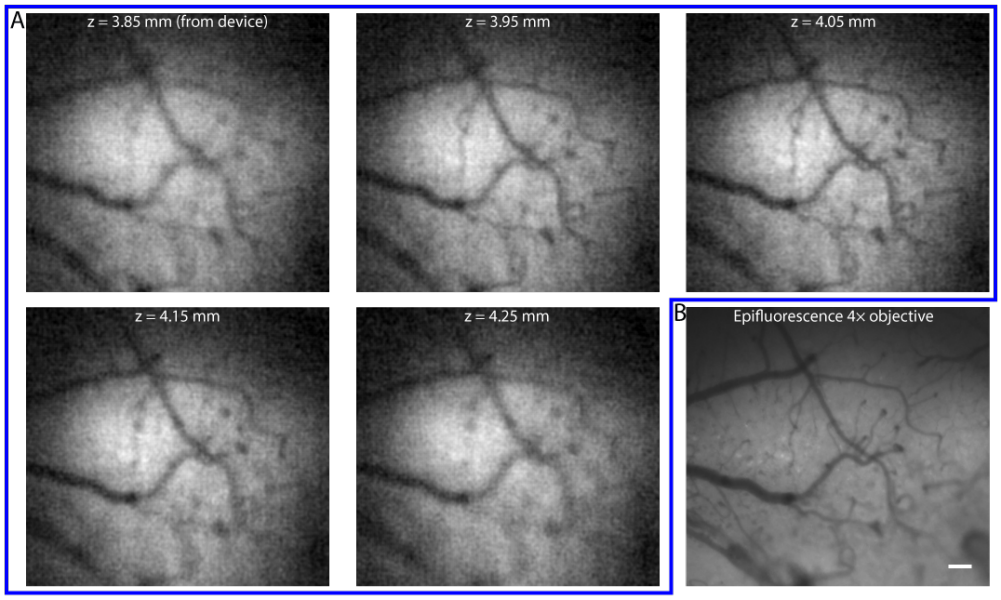

Fig. S11. Digitally refocusing in mouse brain. (A) Bio-FlatScope reconstructions for five different depth planes. At 4.05 mm, the image becomes sharpest for the FOV. (B) Epifluorescence image for the same FOV. Scale bar, 100 µm.

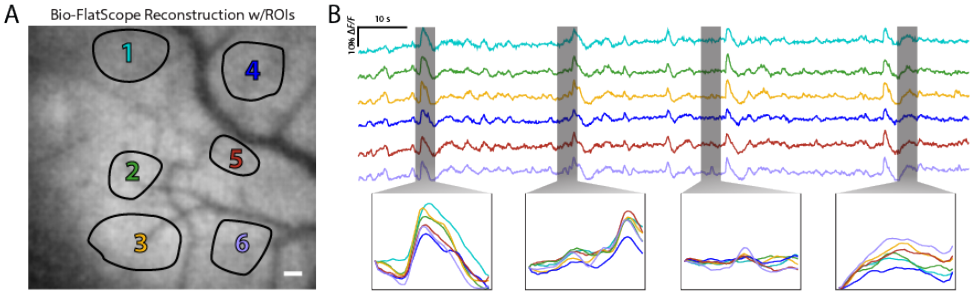

Fig. S12. Ca^{2+} responses from Bio-FlatScope recording across multiple ROIs. (A) Bio-FlatScope reconstruction showing multiple ROIs. Scale bar 100 µm. (B) ΔF/F traces for the multiple regions with zoom-ins showing differences in activity across ROIs.

Fig. S13. Oral mucosa imaging setup, including a chin-head rest and a liquid light guide connected to a tabletop LED source for illumination. This photo shows how the liquid light guide is mounted in the chin rest.

Table S1. Comparison of Bio-FlatScope to miniaturized, head-mounted microscopes.

Microscope[a]	Lateral resolution	Field of view
Bio-FlatScope	~8.8 µm	~16.2 mm^2
Integrated miniature microscope [5]	~2.5 µm	0.48 mm^2
Fiber bundle microscope [6]	~4.9 µm	~0.3 mm^2
Two-photon miniaturized microscope [7]	0.64 µm	~0.03 mm^2
Miniaturized light-field microscope [8]	6 µm	~0.42 mm^2

[a]Selected microscopes have cellular resolution capability and remain light enough (< 3 g) to be mounted on a mouse and allow free behavior without any support.

References

1. J. K. Adams, V. Boominathan, B. W. Avants, D. G. Vercosa, F. Ye, R. G. Baraniuk, J. T. Robinson, and A. Veeraraghavan, "Single-frame 3D fluorescence microscopy with ultraminiature lensless FlatScope," Sci. Adv. **3**, e1701548 (2017).

2. N. Antipa, G. Kuo, R. Heckel, B. Mildenhall, E. Bostan, R. Ng, and L. Waller, "DiffuserCam: lensless single-exposure 3D imaging," Optica 5, 1 (2018).
3. Tajima, K., Shimano, T., Nakamura, Y., Sao, M. & Hoshizawa, T. Lensless light-field imaging with multi-phased fresnel zone aperture. in 2017 IEEE International Conference on Computational Photography, ICCP 2017 - Proceedings (Institute of Electrical and Electronics Engineers Inc., 2017). doi:10.1109/ICCPHOT.2017.7951485
4. Stork, D. G. & Gill, P. R. Optical, Mathematical, and Computational Foundations of Lensless Ultra-Miniature Diffractive Imagers and Sensors. International Journal on Advances in Systems and Measurements 7, 201–208 (2014).
5. K. K. Ghosh, L. D. Burns, E. D. Cocker, A. Nimmerjahn, Y. Ziv, A. E. Gamal, and M. J. Schnitzer, "Miniaturized integration of a fluorescence microscope," Nat Methods 8, 871–878 (2011).
6. M. Kim, J. Hong, J. Kim, and H. Shin, "Fiber bundle-based integrated platform for wide-field fluorescence imaging and patterned optical stimulation for modulation of vasoconstriction in the deep brain of a living animal," Biomed. Opt. Express **8**, 2781 (2017).
7. W. Zong, R. Wu, M. Li, Y. Hu, Y. Li, J. Li, H. Rong, H. Wu, Y. Xu, Y. Lu, H. Jia, M. Fan, Z. Zhou, Y. Zhang, A. Wang, L. Chen, and H. Cheng, "Fast high-resolution miniature two-photon microscopy for brain imaging in freely behaving mice," Nat Methods 14, 713–719 (2017).
8. O. Skocek, T. Nöbauer, L. Weilguny, F. Mart\'ınez Traub, C. N. Xia, M. I. Molodtsov, A. Grama, M. Yamagata, D. Aharoni, D. D. Cox, P. Golshani, and A. Vaziri, "High-speed volumetric imaging of neuronal activity in freely moving rodents," Nat. Methods **15**, 1–4 (2018).